Local microstructure-properties model for HPVDC Aural™-2 using image analysis and machine learning

Gariépy, A.; Tu, S.; Gagné, M.-O.; Samuel, E.

Publisher's version / Version de l'éditeur:

2022 NADCA Die Casting Congress & Tabletop, 2022-09-13

2022 DIE CASTING CONGRESS & TABLETOP
NADCA
NORTH AMERICAN DIE CASTING ASSOCIATION

Local microstructure-properties model for HPVDC Aural™-2 using image analysis and machine learning

A. Gariépy, S. Tu, M.-O. Gagné, and E. Samuel
National Research Council Canada, Saguenay, Canada

ABSTRACT

High-integrity die castings require controlled strength and ductility for structural applications. These properties are the product of the local microstructure of the material after die filling and solidification. In this paper, a workflow of metallographic imaging, image analysis, and machine learning is investigated to estimate the mechanical properties at specific locations in a casting based on the local microstructure. Approximately 180 tensile specimens were first extracted from high pressure vacuum die cast Aural™-2/F plates at 1.8, 3.0 and 4.7 mm thickness and tested. Cross-sectional optical micrographs were then taken close to fracture locations at different magnifications to observe the microstructure. Image analysis routines were developed and applied to systematically quantify the key microstructural characteristics that are expected to affect strength and ductility. Challenges related to sampling of multi-scale and heterogeneous material, imaging resolution, high-volume analysis automation, and statistical descriptions were addressed to seek out compromises between characterization effort and accuracy. Finally, the predictive capability of different families of machine learning algorithms was tested with the dataset of the extracted microstructural characteristics for yield strength, elongation at break, and area reduction at fracture. Feature importance was also evaluated to determine key microstructural characteristics used in correlations. This work therefore assesses the potential for local, destructive estimation of expected in-service mechanical behaviour, for instance in regions where tensile coupons cannot be extracted. Validated relationships between microstructure and properties could also eventually complement simulation-based microstructure predictions from process parameters in an integrated computational materials engineering framework for designing new, lightweight die-cast structural components.

INTRODUCTION

High-pressure vacuum die casting (HPVDC) can be used to produce large series of complex, structural components, for instance for automotive applications. This net-shape process can create varying sections within a single part which, combined with alloy selection and process-dependent filling and solidification factors, can lead to varying mechanical properties within as well as between parts. For structural applications, understanding and controlling these variations is important to consistently achieve the required service performance.

Strength can efficiently be estimated locally using indentation-based methods, but ductility is more challenging to assess in sections that are not well-suited to tensile or bend tests. The local properties are a result of the local microstructure. As such, characterizing the microstructure of specific regions in a given casting could therefore provide estimates of their associated mechanical properties. While metallographic characterization is as destructive a test method as mechanical testing, it could be applied in small, irregular regions such as the edge or base of structural ribbing as illustrated in Figure 1.

Figure 1: Example of an irregular section on a prototype casting after destructive testing

For common Al-Si-Mg-Mn structural die casting alloys, the microstructure consists of a distribution of coarse primary and fine aluminium, eutectic regions, intermetallics, and precipitates arising from solidification and heat treatment, in addition to potential defects such as porosity, oxides or other inclusions [1]. These microstructural features depend on the processing conditions and affect mechanical properties. Many relationships have been identified, discussed, and controlled in the literature. The effects of alloy composition on strength and expected ductility are well mapped towards material selection for specific applications [2]. Similarly, the effects of grain size and secondary dendrite arm spacing on strength and ductility have been widely investigated [2-5]. While yield strength is mostly related to metal composition, cooling rate, and heat treatment, ductility and as a result ultimate tensile strength are affected by a wider range of microstructural features. For instance, it is well documented that the presence of micro- and macro-porosity is detrimental to ductility and fatigue life by acting as favourable strain localization and crack initiation points [5-11]. Elongated, needle-like intermetallic constituents and eutectic silicon are also known to reduce ductility depending on their morphology [5, 11-15], which have led to the development of low-iron and strontium-modified structural alloys. Large, externally-solidified primary aluminium crystals (ESCs) represent local inhomogeneities that affect material deformation and are reported to bring about a reduction of static ductility in thin-walled parts; efforts were made to reduce their occurrence especially in magnesium die casting [6]. Many of these factors are also interrelated: for example, intermetallic compounds or eutectic evolution also have an impact on material feeding and porosity formation in different casting processes [5, 16-18]. Similarly, the distribution of ESCs can alter flow and induce local microporosities at solidification leading to a compound, detrimental effect [19-23]. Finally, within the already heterogeneous microstructure, occasional oxides, inclusions, or cold flakes originating upstream from the cavity [24-26] or filling defects like cold shuts [27, 28] can be significantly detrimental to ductility [29]. While the investigations referenced here provided valuable insight regarding the specific factors controlling die casting quality, they often focused qualitatively or quantitatively on either a single or a few features. Limited studies have been undertaken to pursue a statistical analysis on *all* of the features mentioned above in order to establish a predictive model capable of mapping microstructure to mechanical properties [15].

Predictive models require quantified inputs. The ability to generate relevant, accurate, and reliable image descriptors of microstructure is the key to extracting the microstructure-properties relationships of materials. Quantifying the microstructural characteristics can be achieved using automated image analysis, especially when dealing with a large number of specimens and micrographs. Digital image analysis techniques have long been applied in material microstructure analysis [30] and algorithms can be developed to capture the many specific features, and their distributions, of die-cast microstructures. For example, image analysis was used to quantify the eutectic fraction profile across cast specimens [31]. More advanced methods can also be applied to detect and size more complex objects such as fracture surface defects [9].

The net-shape nature of die casting could lead to probabilistic variations and interactions between microstructural factors [6, 7, 16, 32]. Ductility, for example, is likely to be controlled by a single or few detrimental instances, which could vary from part to part due to the inherent variability in turbulent filling and probabilistic aspects of defect occurrences and solidification [9, 33]. This makes developing quantitative models challenging. Artificial intelligence is an active topic of research in die casting, especially with a focus on binary classification for part quality. For instance, Blondheim leveraged extensive process data from multiple sources to predict pass/fail quality after machining for 1873 parts from casting process inputs over a week of normal production [34]. In follow-up investigations, clustering algorithms and signal analysis were applied to anomaly detection [35, 36]. The results highlighted the interest of advanced algorithms to find patterns in large sets of complex, interrelated data. Similarly, Liu *et al.* tested the applicability of machine learning algorithms such as neural networks and gradient boosting to analyze scrap rate and predict quality from process parameters for a dataset of 345,000 parts [37]. In another study, Apelian and Kopper applied tree-based models to predict the good/scrap classification of over 950,000 parts with 83 inputs and outputs from the cell in a production environment, and addressed the challenges of imbalanced and missing data in materials processing [29, 38]. These large samplings fit well with the "big data" requirement of some advanced machine learning models. Machine learning can also be applied in regression analyses to predict a continuous value. For instance, Kopper implemented multiple algorithms, as well as principal component analysis, to predict the ultimate tensile strength of 1500 specimens from process data. Artificial intelligence appears to be an interesting avenue for predictive tools for microstructure-properties relationships, as an alternative to complex physics-based computations [7]. However, developing microstructure-to-properties relationships is likely to rely on a relatively small number of specimens, which will bring challenges specific to low-volume data.

Within a broader project seeking to estimate die casting properties early during design, this paper focuses on the development of a predictive framework from microstructure characterization to mechanical properties using machine learning. The intent is to use process simulations to predict relevant microstructural features [25,39-41], and then estimate mechanical properties from these material characteristics. Microstructure-properties correlations could also be used to estimate the strength and ductility of irregular regions that are difficult or impossible to test using conventional tensile or bending methods. The methodology was developed with the Aural™-2 alloy, which is commonly used for high-integrity components in the automotive sector, using as-cast stepped plates covering a range of thicknesses typical of thin-walled, structural parts. The first objective was to extract the relevant microstructural features, including their distributions, from micrographs with large fields of view. Using digital image analysis techniques, the microstructures were then quantified in an unbiased and automated manner, which can be readily scaled up. The second objective was to select and tune machine learning models to relate these features to the measured strength and ductility from tensile testing, in order to evaluate the potential gain in predictive capability with this method.

EXPERIMENTAL METHODS

HPVDC EXPERIMENTS

In this investigation, flat, stepped plates were cast under varying HPVDC process conditions on the NRC's research and development cell. The plates, illustrated in Figure 2a, had sections measuring 4.7, 3.0 and 1.8 mm in thickness and were cast using the same die as the authors' previous investigation on microstructure modelling [42]. The cell surrounding the 530-ton Bühler SC N/53 cold-chamber die casting machine has automated metal ladling and spray functions as well as a Fondarex HighVac/ExVac 500 L vacuum system (Figure 2b). In all experiments, the melt was held in an electrically heated crucible furnace, fluxed with a Wedron metal treatment system, and degassed with argon.

(a) (b)

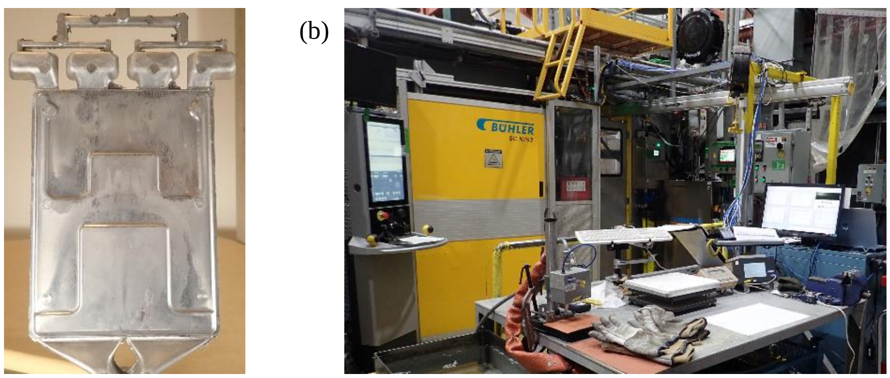

Figure 2- (a) Cast plate used to extract tensile coupons. (b) General view of the die casting R&D cell.

All casting trials were conducted with an Aural™-2 alloy, with the measured range of composition shown in Table 1. The objective was to keep the alloy composition as stable as possible throughout the experiments in order to focus on process-induced variations. It is well known that actual alloy composition is a significant factor that can influence the mechanical behaviour: this topic was however outside the scope of the work presented here. After comparing properties in the as-cast (F) temper and heat-treated (T7) tempers, it was decided to investigate the process-induced F-temper variability only.

Table 1- Alloy composition range during 7 days of casting trials over 4 months, in % mass

Aluminum	Silicon	Magnesium	Iron	Manganese	Titanium	Strontium
Bal	10.3-10.9	0.29-0.32	0.18-0.20	0.48-0.51	0.06	0.010-0.016

To generate a range of typical and detrimental process conditions, die thermoregulation temperature, melt holding temperature, fast shot velocity, vacuum level, shot mass, and cycle time were varied in the ranges shown in Table 2. Moreover, the remelt fraction in the crucible was varied between 0% (all primary ingots) and 50%. Remelt was taken from the feeds and overflows from previous castings with the same alloy: the iron content therefore remained quite stable. In the specimens selected for testing, the intensification pressure target was constant at 500 bar.

Over 900 tensile specimens based on the ISO 6892 standard [43] were extracted from the cast plates for testing to investigate the process-properties correlations as part of a wider project. Displacement-controlled tensile testing was performed on an MTS Alliance electromechanical machine with a 25-mm gauge length extensometer. After testing, the area reduction at fracture was also calculated for each specimen as a local ductility measurement compared to elongation at break over the entire gauge length.

Table 2- Range of die casting process parameters in this work

Parameter	Upper and lower bounds
Die thermoregulation temperature	180-255°C
Melt temperature	670-720°C
Metal velocity at gate	25-50 m/s
Vacuum level	55-300 mbar
Cycle time	70-120 s
Biscuit length	17-23 mm

METALLOGRAPHIC CHARACTERIZATION AND IMAGE ANALYSIS

From these specimens, a subset of 189 units were specifically selected for systematic metallographic characterization. These covered the range of yield strength and ductility from the mechanical testing results, but also included many overlaps as different process parameters can lead to similar properties.

The first step was to determine *where* to characterize the specimen microstructures. Given that there is no to minimal thermomechanical processing done after forming, aluminium die casting can exhibit local microstructural variations. For example, the exact locations of porosity instances can vary slightly from one shot to another [34]. Similarly, rare, isolated defects such as cold flakes tend to affect a small, localized volume of material when they occur in parts. Selection of metallographic sampling plane and regions of interest is therefore important to relate the observed microstructure to the mechanical properties measured in testing. In this project, it was decided to image and characterize a single plane nearly parallel to the fracture plane in a deformed region on the tensile specimen, at a minimal distance of a few millimeters away from the fracture surface. This was justified as larger defects tend to cause strain localization and fracture and bulk observations may not correlate well with measured properties [9,33]. The method to characterize the fracture-adjacent material was expected to provide a better specific estimate of the properties of the detrimental region especially for ductility, at least in a statistical sense. The drawbacks of this method are the observation of a stretched microstructure and the potential to capture testing-induced voids. However, since this investigation focused on the F-temper with a relatively low area reduction at break compared to T7-treated Aural™-2, these limitations were deemed acceptable. Another option would be to sample undeformed material taken further away from the fracture location, at the risk of missing important, local characteristics.

Once metallographic preparation of the selected cross-section was concluded with 0.25-µm oxide polishing, the specimens were imaged using an Olympus BX-51 optical microscope equipped with a Clemex color CCD camera, with consistent control of illumination and without chemical etching. The well-known skin effect in die-cast aluminium [11,24,44,45] and segregation band of increased eutectic fraction related to dilatant shear [22,31,46] caused through-thickness variations of microstructure: images were therefore systematically captured from one surface to another. In the perspective of automation, the specific regions of interest on the 5-to-9-mm-wide section plane were pre-determined and not manually adjusted to capture potentially detrimental features.

The selection of image descriptors was based on the analysis of solidification process and the resulting microstructure. In cold-chamber HPVDC, the melt is poured into the shot sleeve where primary α-Al starts to solidify from liquid along the chamber wall, and subsequently grow into the coarse ESC. The plunger then begins its slow shot to avoid air entrapment and provide time for vacuum to be established in the cavity. As the alloy approaches the gate, the plunger accelerates to its fast shot velocity to fill the cavity, where air can also be entrapped leading to porosity. During and after filling, contact with the steel die under high pressure leads to fast solidification of the primary aluminium in fine globular or rosette morphology [47] between the ESCs. As the temperature drops below the eutectic temperature, the remaining melt solidifies as eutectic regions containing fine silicon particles between the already-solid primary aluminium. Throughout this process, the die casting machine applies high pressure to feed material (before the gates freeze) and minimize jagged, sponge-like shrinkage porosity [16]. Intermetallic compounds also form in the microstructure due to the presence of iron and manganese in the alloy [17]. Optical micrographs were taken at 100X and 200X magnifications to capture the features of this multi-scale, multi-phase structure, as shown in Figure 3. The lower magnification images were stitched together to generate a single mosaic [24] which was analyzed for coarser microstructural features such as ESCs or eutectic agglomerations, including their locations through-thickness. These large-scale mosaic images were taken to sample as much of the material as possible. The higher magnification images were used to quantify the finer characteristics at 64 to 144 locations, depending on thickness, evenly spaced on the region of interest. In this investigation, it was decided to only use medium-magnification optical imaging to minimize the characterization effort towards potential industrial applications. As a result, the eutectic characteristics were only measured collectively due to the fact that the typical individual silicon particles were in the sub-micron range, which is difficult to quantify accurately with optical microscope. The downstream model range of applicability will therefore be limited to the alloy under investigation, especially in terms of eutectic modification, as a potentially significant factor for mechanical properties is not included. Higher-magnification optical imaging, electron microscopy or differential scanning calorimetry can provide further information on very fine features such as eutectic silicon and nano-scale precipitates, but these are generally time-consuming to achieve quantitatively at the large volume required in this investigation.

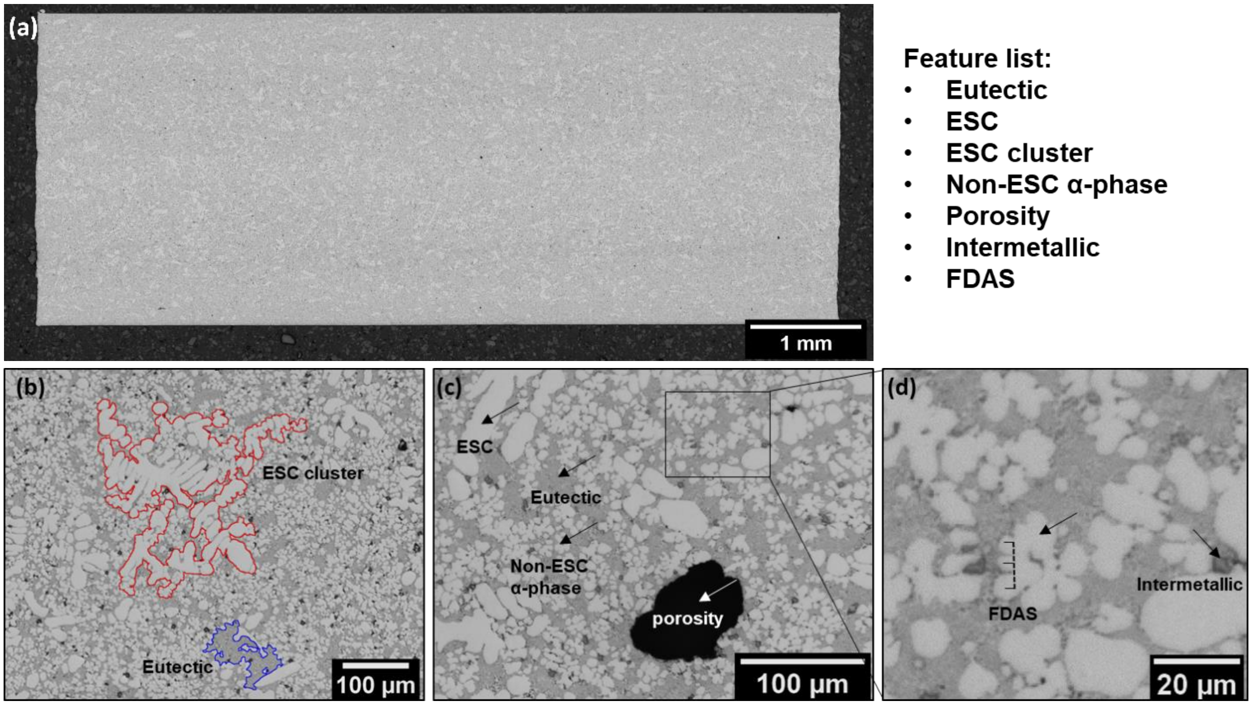

Figure 3- (a) Low magnification stitched image of 3-mm thick Aural™-2 alloy cross-section near fracture surface after tensile test. (b-c-d) Higher magnification images with indication of (b) an ESC cluster (red) and a eutectic region (blue) considered as a large eutectic segregation, (c) ESC, eutectic, non-ESC α-phase and porosity, and (d) magnified view with FDAS schematics and intermetallic constituent.

Once consistent images were captured, they were analyzed using automated image analysis. After carrying out normalization steps to allow direct comparisons between images and calibrating the scales to extract features in physical units, routines were developed to identify individual instances of each feature of interest and extract key numerical characteristics towards machine learning based on the literature and industrial background. In addition to common measurands such as average area, aspect ratio, or area fraction for each feature of interest, advanced shape and statistical analyses were also conducted for some elements [10, 16, 17, 24]. For instance, the Sauter mean diameter d_{32}:

$$d_{32} = \frac{\sum_i d_i^{\,3}}{\sum_i d_i^{\,2}}$$

where d_i is the equivalent diameter of a circle with the same area of an individual instance i, was used instead of the arithmetic mean to weight the individual instances with their area. Since ductility can be affected by a few, extreme instances [11], upper-bound estimates such as the maximum or 95th percentiles were also extracted. Due to the complex morphologies, advanced algorithms such as watershedding and fractal dimensions were integrated in the analysis routines to quantify the observations, for instance for the regions shown in Figure 3b. The spatial distributions of instances can also be a factor for mechanical behaviour as clusters of individual instances can be more detrimental [7, 9]. Some features were evaluated in subsets of the metallographic images to identify possible concentrations. Quantitative clustering metrics were, however, not implemented herein [48]. It is worth noting that automated image analysis often still involves user decisions, for example when selecting grayscale thresholds for phase distinctions [48] or determining lower-bound size threshold to remove artefacts or irrelevant instances. In this work, a systematic approach was followed to ensure comparable imaging and analysis throughout, to avoid introducing bias into the downstream modelling activities.

Many investigations have included fractographic analysis of the fracture surfaces in correlations [9, 28]. This was also conducted in this work, but the results were not included in the machine learning models, as having a fracture surface implies prior mechanical testing. With the objective of evaluating properties from microstructure alone, for instance in regions where mechanical testing is not practical, information on fracture surface defects or morphology would not be available. Fractography was therefore considered as post-modelling information to relate to the predictions.

ImageJ® and Python® were used to perform the digital image analyses for all the image descriptors. Given the evolving nature of the analyses, and the more than 10,000 images database, batch processing of images and generation of a grouped datasets were programmed for efficiency. As the analysis routines evolved frequently in development to cope with the new challenges in newly acquired images, version tracking was implemented and a consistently-processed, comparable dataset was extracted for modelling.

MACHINE LEARNING MODELS

Machine learning spans a variety of mathematical and statistical models and includes a range of preparation and post-processing tasks [29]. In this project, the Python language and its suite of machine-learning-oriented modules such as scikit-learn and the user-friendly PyCaret® library was used for computations.

After grouping all the sources into a single dataset, the first task generally involves human intervention to analyze the data at hand. The variable types detected by the software were first verified: in this study, all predictors (the microstructural characteristics) and targets (the measured mechanical properties) were numeric. The dataset was then checked for missing data: in this case, no imputation was required. Even with the relatively small number of lines in this investigation, data analysis was done first in a statistical sense, to identify the variance of each predictor and any potential outliers or trends or groups in the distributions. This step identified individual image analysis challenges leading to an iterative refinement of the characterization routines. Additionally, correlations between single predictors and targets could already be identified here. For instance, since multiple statistical indicators were included for some microstructural features and some features were cross-correlated, some predictors among the 70 originally extracted in image analyses exhibited noticeable correlations, which can be detrimental especially for some models [34] and can be detected using tools such as the variance inflation factor.

In order to test the models to be developed, the complete set was split into training, testing and unseen sets based on the PyCaret® workflow. The training set was first used to compare and tune different model types using a cross-validation method. The predictive accuracy can then be evaluated by introducing the testing set and calculating the quality of the new predictions in order to select promising algorithms. Finally, new models of the same types can be defined using both the training and testing sets. The unseen sets included 15% of the available data and represent the application use-case of introducing new data to an operating model to get its predictions. Given the small dataset and the relatively large variation of strength and ductility, four unique and constant training/testing/unseen sets were generated to evaluate the reproducibility of the results with different splits. Furthermore, each unseen set was constructed so as to sample the range of the measured ductility by randomly selecting lines in sub-groups of increasing ductility.

The second step involves pre-processing. The pre-processing requirements depend on the type of data and the models to be used. For instance, linear and K-nearest-neighbours (K-NN) models can be sensitive to the range of values and the absolute values of predictors in this work ranged from the order of 0.01 to 100,000. Data was therefore normalized for compatibility with a variety of models to be evaluated. Furthermore, initial data exploration showed that many predictors had non-normal, skewed distributions with a tail of larger instances inherent to the process. Since many models are known to perform better with predictors having Gaussian-like distribution [49], power transforms such as Box-Cox and Yeo-Johnson were also tested. In addition, principal component analysis (PCA) can be a useful method when dealing with correlated predictors [29]. This method generates new, linearly independent and ordered predictors, at the expense of reduced model explainability. While explainability was an important goal in this investigation to interpret the results, PCA was tested as a means to handle correlated predictors with minimal intervention as part of automated machine learning applications. Finally, given that the low-ductility specimens still represented a relatively small fraction of the dataset, but an important one to capture for quality purposes, weighting factors based on the prior distribution of the target were also generated for modelling trials. The purpose here is similar to the synthetic minority oversampling technique (SMOTE) that can be used to improve accuracy for imbalanced data [29,38].

The data was then input into machine learning models to compare the relative performance of different groups of algorithms [29,34]. In this work, the PyCaret® library was first used to quickly assess a large number of models using built-in functions and simple programming to loop over different predictor selections, preprocessing options, or training/testing/unseen sets. Given the small number of data lines, each parallel computation took less than 5 minutes on a portable workstation equipped with an Intel i7 processor and many variations could be efficiently tested overnight to determine favourable modelling options. Throughout all of the computations, random number generation was controlled to ensure reproducible analyses: this is especially important in models involving stochastic decisions, such as random forests.

Further tuning was conducted to maximize the accuracy of a small number of retained models. The optimal hyperparameters, such as the number of tree or tree “complexity” in tree-based models or learning rate in boosting models, depend on the extent and type of input predictors and can be adjusted. In this work, after identifying reasonable ranges from random grid searches on PyCaret®, final tuning was conducted by a dedicated data scientist with experience in this field. An important aspect of tuning is control of over- or underfitting. The application of some models, especially those using boosting strategies, on small datasets such as the one in this work can lead to overfitting with excellent predictions on the training set but poor performance on new data as the model tries to capture small, noisy variations in the trends [29].

The tuned models were then run with the unseen data to evaluate the expected predictive capability in terms of the root mean square error (RMSE) and R^2 coefficient. The model output was also analyzed in terms of feature importance [29] and explainability [50], to gain insight into the predictors having the most impact on the predictions and confirm which features would be of most importance to measure (and eventually predict) to estimate strength and ductility.

RESULTS AND DISCUSSION

FEATURE ENGINEERING

A total of 70 predictors were extracted for each specimen to describe the coarse and fine aluminium, eutectic, intermetallics, and porosity in terms of average dimension, shape, extreme dimension, and relative area occupation.

Figure 4 shows typical distributions of externally-solidified crystals, intermetallics, and porosity instances quantified through automated image analysis in three example specimens. Each specimen reveals different characteristics from the others, which shall be used for correlations with the resulting properties. The intermetallics and ESC distributions are noticeably asymmetrical with the presence of larger instances. These are related to the statistical aspects of solidification in the cold chamber and inside the cavity. Porosity typically exhibits a more jagged distribution caused by the occasional presence of a single or few much larger instances in addition to microporosity, especially in the thicker specimens. It should be noted that the two-dimensional metallography only presents a cross-section whereas structures, especially large ESCs and shrinkage porosity, are in reality three-dimensional. Areas that appear disconnected on the section may in fact be interconnected, which necessitated appropriate image analysis functions to best estimate likely groupings from the available 2D data.

To account for these skewed microstructural characteristics and the expected importance of the extreme values on ductility, upper-bound values were extracted for some features, including the 95th percentile, 99th percentile and maximum value from the individually detected instances. Figure 5a-b illustrates the relationships between average and extreme values of ESCs and porosity also with respect to section thickness for the complete dataset. Higher average values typically correspond to higher extreme values, but the Pearson correlation coefficient remains relatively low on the order of 0.45 to 0.6. The correlation between average and upper bound evaluators generally degraded and the noise increased when increasing the percentile, as the upper bound evaluator became more sensitive to single, extreme instances in the microstructure.

There is also a correlation between some predictors of different categories. For instance, the general trend between dendrite arm spacing and intermetallics in Figure 5c, notwithstanding some outliers such as the top right point, can be associated with their common dependency on the average cooling rate which is dependent upon section thickness that is defined by product design. The location within the casting can also be a factor, for example for externally-solidified crystals [22], but this factor cannot be effectively decoupled from thickness in this work. The differences within a group can be associated with variations of cooling rate from process factors, most importantly from the die thermal management. The fine dendrite arm spacing metric developed herein for the fine cavity-solidified α-aluminium is an alternative estimator to the conventional secondary dendrite arm spacing that becomes challenging to evaluate, especially for high-volume automation, for the morphologies that arise from the fast cooling rate in HPVDC [47]. Compared to previous studies spanning multiple casting processes or wide ranges of cooling rate [4], this investigation focused specifically on HPVDC, which resulted in a much narrower grouping of DAS values that could make correlations with properties more difficult. Further investigation of the group of points at the bottom left of Figure 5c revealed that analysis of these specimens was biased by the presence of more scarcely distributed eutectic particles between which the aluminum just passed the threshold and was regarded as very fine dendrite by the image analysis algorithm, leading to relatively lower DAS results. This leads to difficulties in determination of ambiguous microstructures during an automatic image analysis campaign where prior experience is not programmed into the algorithm. This highlights the importance of the iterative approach applied in this work for image analysis development where in each iteration the outliers are to be verified in detail to fine-tune the algorithm.

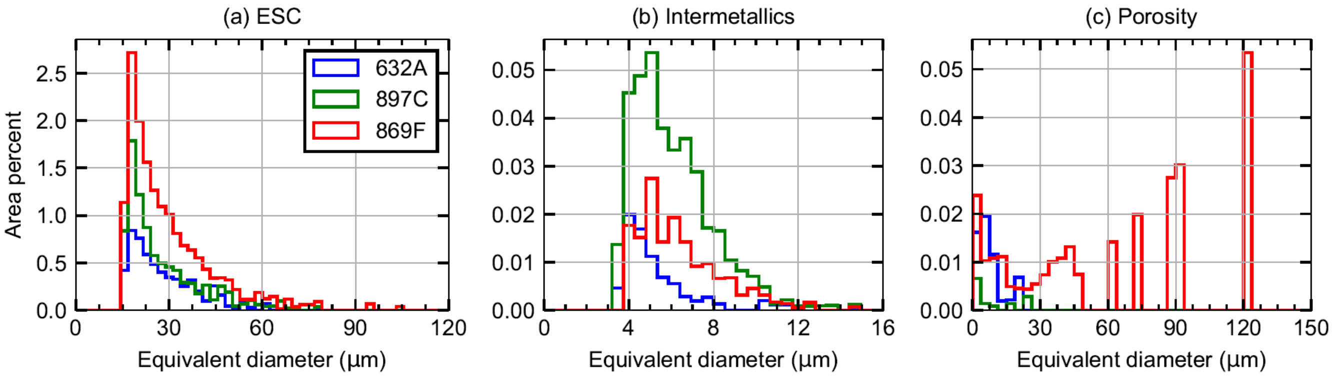

Figure 4- Examples of distributions of (a) externally solidified crystals, (b) intermetallics and (c) porosity from image analysis. Specimens correspond to different thicknesses as well as different process parameters.

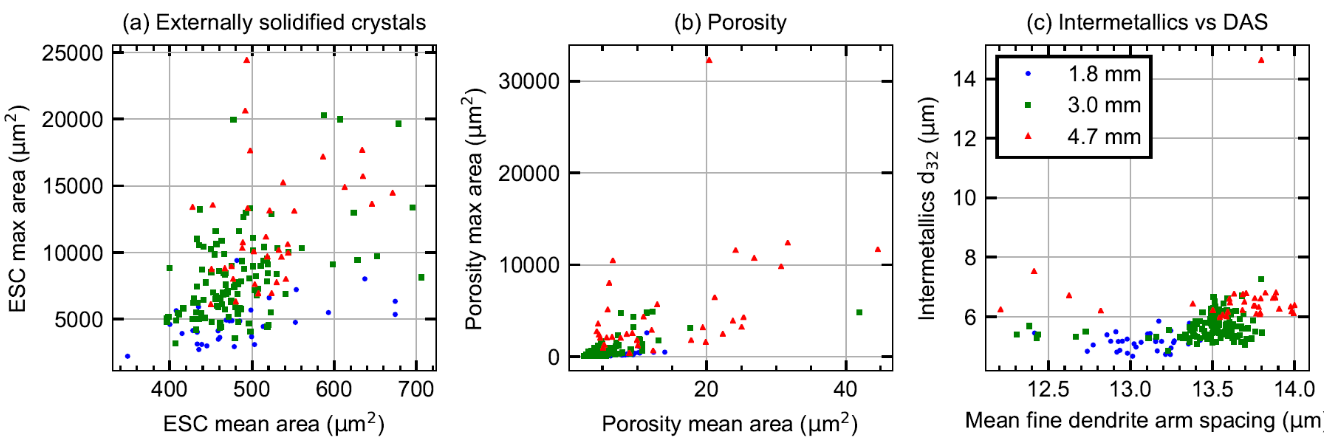

Figure 5- Correlations between selected predictors from automated image analysis. (a-b) Relationship between average and maximum evaluators for ESC and porosity. (c) Relationship between cavity-solidified dendrite arm spacing and intermetallics dimensions.

DATA EXPLORATION

Visual analysis of the direct correlations between predictors (i.e. microstructural characteristics) and targets (mechanical properties) already highlights some trends. For instance, Figure 6 presents individual relationships between yield strength and dendrite arm spacing, intermetallics size or ESC area occupation. Each shows a trend for decreasing yield strength with increasing predictor value, with Pearson coefficients between 0.3 and 0.7. Each predictor by itself is therefore not sufficient to estimate the property of interest. It should also be noted that Figure 6 illustrates correlations, not causations. For instance, the intermetallic constituent mean area is not expected to be such a significant factor to the yield strength: it can however be a metric of the cooling rate and solidification history that control many other, potentially more mechanically significant, microstructural characteristics.

Trends on ductility tend to be more complex, as illustrated in Figure 7. As expected, larger instances of porosity, which also correlates with a higher area occupation, correspond to a reduced elongation at break. Interestingly, the correlation between porosity and area reduction at break was not as good, as porosity may have a more significant effect on localization of deformation on the gauge section. The presence of externally-solidified crystals, especially in the skin regions, also exhibits a similar trend as well as grouping of the specimens with similar thicknesses. Eutectic solidification can play a major role in high-silicon hypoeutectic alloys such as Aural™-2. Concentration of Al-Si eutectic in large regions is of interest as the eutectic is generally more brittle than the α-phase and large clusters are expected to decrease the ductility of the material. This trend appears in Figure 7c. It can be seen that a significant presence of these features tends to correspond to lower-ductility specimens. On the other hand, the absence of one of these features does not necessarily correspond to high ductility, as other detrimental microstructural characteristics could be present and limit ductility [9]. These competing mechanisms could be a challenge for simpler models such as multiple regression [15].

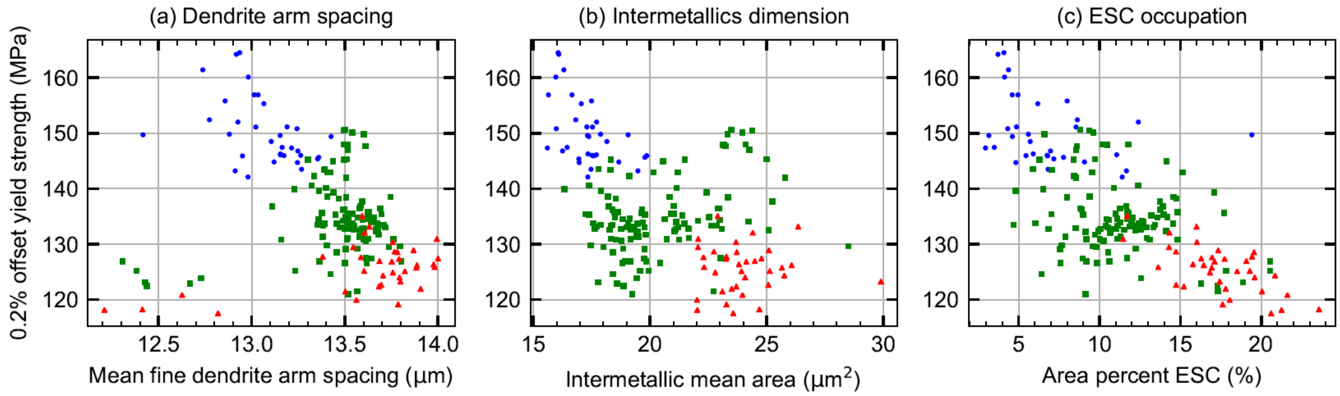

Figure 6- Individual scatter plots illustrating the correlation between yield strength and (a) dendrite arm spacing, (b) intermetallics dimension and (c) ESC area occupation. Colour-coding is the same as Figure 5.

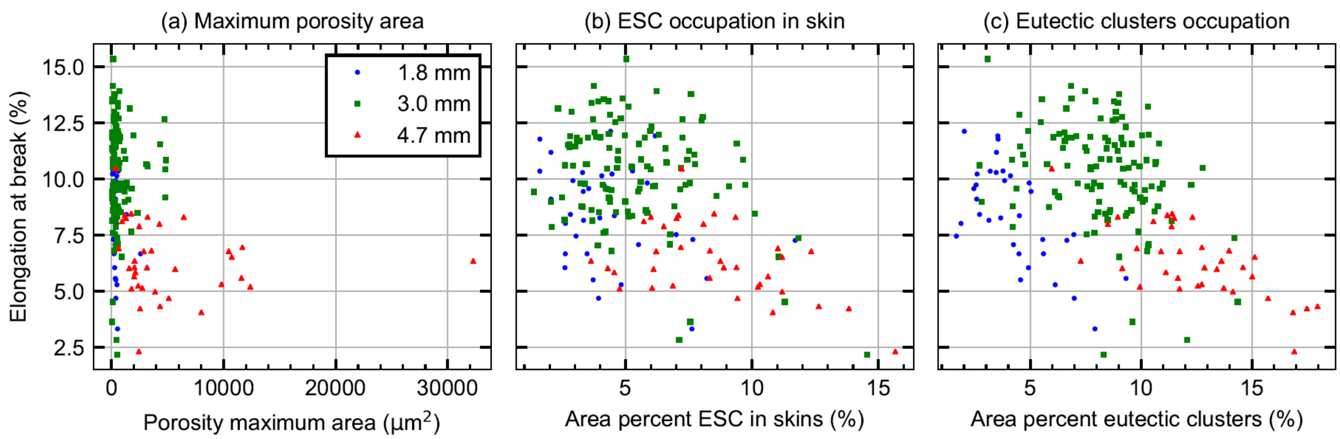

Figure 7- Individual scatter plots showing the correlation between elongation at break and (a) maximum area of a single porosity instance or (b) area occupation of ESCs in skins and (c) eutectic clusters.

MACHINE LEARNING MODELS

Figures 8 and 9 summarize some of the initial comparison of models on PyCaret in terms of root mean square error on yield strength and area reduction, respectively, using various versions of the complete dataset with all features:

1. Original: only a robust scaler is applied to all features prior to the modeling;
2. Box-Cox: the features are transformed using a min-max scaler followed by a Box-Cox power transform;
3. Yeo-Johnson: the features are transformed using a standard scaler followed by a Yeo-Johnson power transform;
4. PCA: principal component analysis is fitted on the original features and the 16 most significant components are retained as the new predictors.

Similarly, four types of model were evaluated: regularized regression refers to linear models such as ridge regression and elastic net and tree-based refers to randomized trees such as random forest. For each combination, the same four different training/unseen splits were run and the average RMSE was calculated.

The four model types performed well on the 0.2% offset yield strength target, as shown in Figure 8, with a root mean square error (RMSE) on the order of 5.5 MPa on the range spanning 118-165 MPa. This corresponds to R^2 values between 0.65-0.8 on the unseen datasets. Linear regressions yielded the best results and the slightly degraded performance of K-NN and tree-based models are likely to be related to occurrence of overfitting. The outliers, such as the Box-Cox results with the K-nearest neighbours algorithm, demonstrate the need to explore multiple modelling strategies to determine the most suitable method.

In terms of area reduction in Figure 9, considering the average on four runs, linear models with the original set of features show a larger error but the power transforms as well as principal component analysis bring significant improvement as expected for this kind of model. Boosting and randomized forest models performed slightly better and yielded similar error with all the versions of the dataset while K-NN further improved the predictive score with the original and PCA datasets. Nevertheless, accuracy was not as good as with the yield strength correlation, with average R^2 values in the range of 0.35 to 0.5 on the unseen datasets. Figure 9 shows a noticeable difference between sets and that some splits proved more challenging for some model types, for instance set # 4 for KNN, which suggests that the relatively small number of training points may not be able to capture a sufficient range of scenarios.

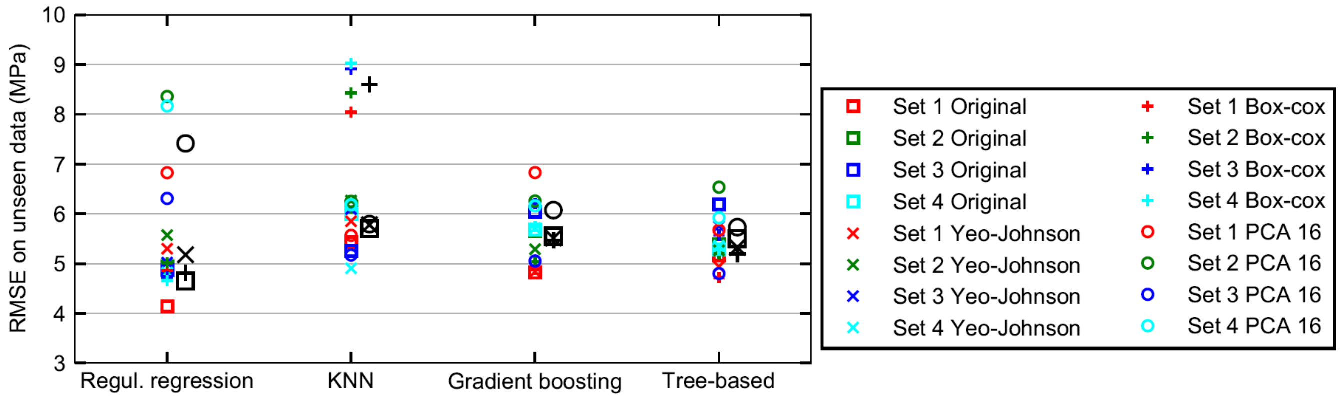

Figure 8- Summary of root mean square error on 0.2% offset yield strength predictions for unseen dataset and different model types and strategies (lower is better). Points in color represent individual training/unseen sets and points in black are the average over the four different sets.

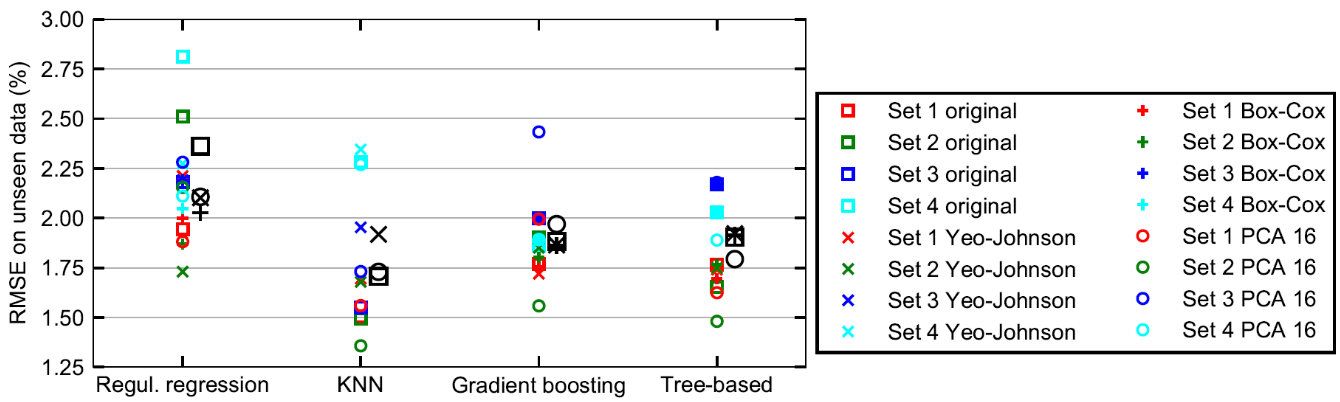

Figure 9- Summary of root mean square error on area reduction predictions for unseen dataset and different model types and strategies (lower is better).

Based on these results, further parameter tuning was attempted to improve the predictive accuracy for the two types of models deemed most promising. The KNeighbors and extra trees (extremely randomized trees, similar to random forest) regressors were retained from the sci-kit learn advanced API but no significant improvement over PyCaret was obtained meaning that the latter successfully found a suitable set of hyper-parameters.

As Figure 10 shows, the distribution of the target variable is imbalanced towards average values despite our effort to deliberately select specimens across the range. Because of this, models like extra trees struggle to predict the extremes, which increases the RMSE metric. To mitigate this problem, weighting factors were added to the training sets to give more importance to the few upper and lower data points to improve accuracy in those practically important ranges. For instance, it would be especially important to detect low-ductility regions for riveting or service performance. Predictive accuracy was indeed improved, as illustrated with the filled symbols in Figure 11. However, a more conservative model, where the predicted ductility is lower than the actual (observed) one, would be desirable. The improvement is visible mostly for the training set, especially when breaking down the RMSE into the different thicknesses as shown in Figure 12. However, the better score for the training set, compared to the unseen set, suggests that some overfitting occurs and is likely due to the small datasets in this investigation. Figure 12 also highlights that the accuracy of the model seems to improve as thickness increases even though all thicknesses are put together in the training process.

The benefit of area-specific modelling can be evaluated by comparing to thickness-specific properties [7,28,51], as shown in Figure 12. Compared to the root mean square error calculated by taking the average value by thickness, the training data shows an approximately 50% smaller RMSE and the unseen data 8-24% smaller RMSE for area reduction at break. There is therefore a potential accuracy gain by using local information on the microstructure. Nevertheless, the relatively higher RMSE on the unseen data suggests a possible overfitting remaining in the analyses.

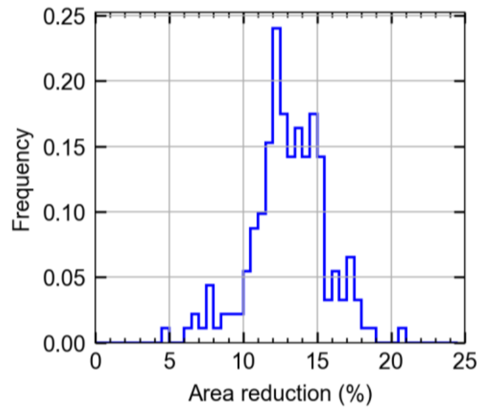

Figure 10- Target distribution for area reduction.

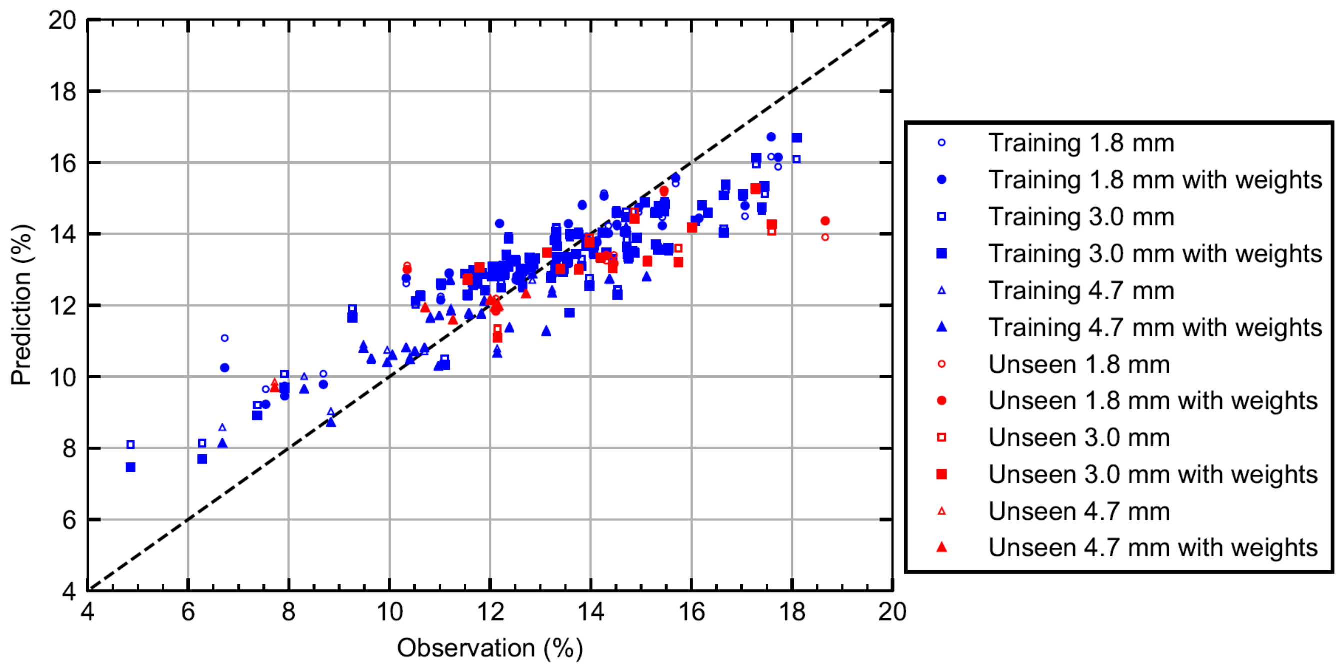

Figure 11- Example of area reduction predictions vs observations with and without sample weights for one training/unseen split.

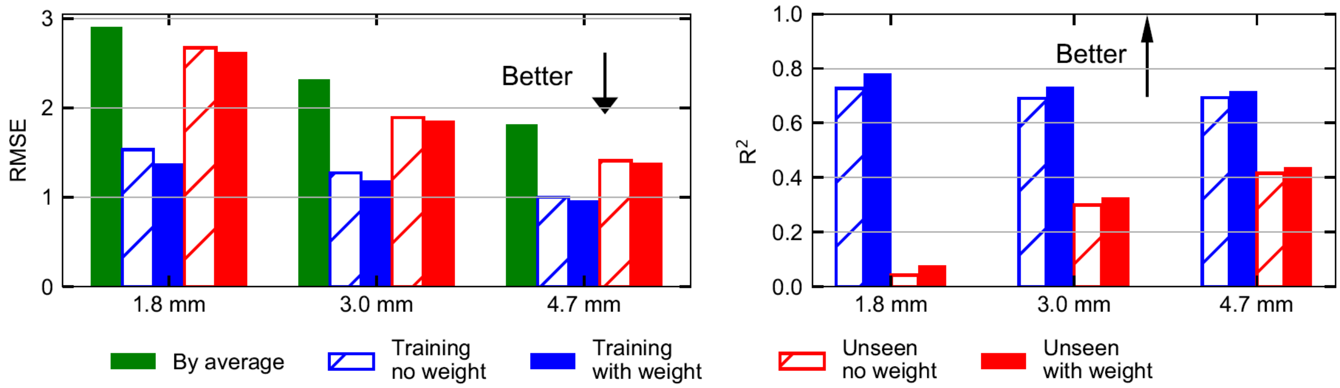

Figure 12: Calculated RMSE and R^2 by thicknesses for training and unseen data, with and without weighting for extra trees model. RMSE calculated using the average value by thickness is provided as a reference.

Given the large number of available predictors from image analysis and the good performance observed when modeling the area reduction with 16 principal components only, further development focused on feature selection to identify the most relevant microstructural features. A typical way to perform feature selection is in a first time by removing collinearities and highly correlated predictors and then using tools like the Boruta method or feature importance analysis after models are fitted with the entire set of features. However in this study a different approach was used based on how the feature engineering is done and the physical meaning of the predictors. Specific predictor groupings were kept and the results are illustrated in Figure 13

1. Average dimension, area occupation and simple shape metrics (14 predictors)
2. Area occupation, d_{32} metric, advanced shape metrics (25 predictors)
3. Area occupation, d_{32} metric, 95^{th} percentile, and advanced shape metrics (40 predictors)
4. Area occupation, d_{32} metric, 99^{th} or maximum, and advanced shape metrics (41 predictors)

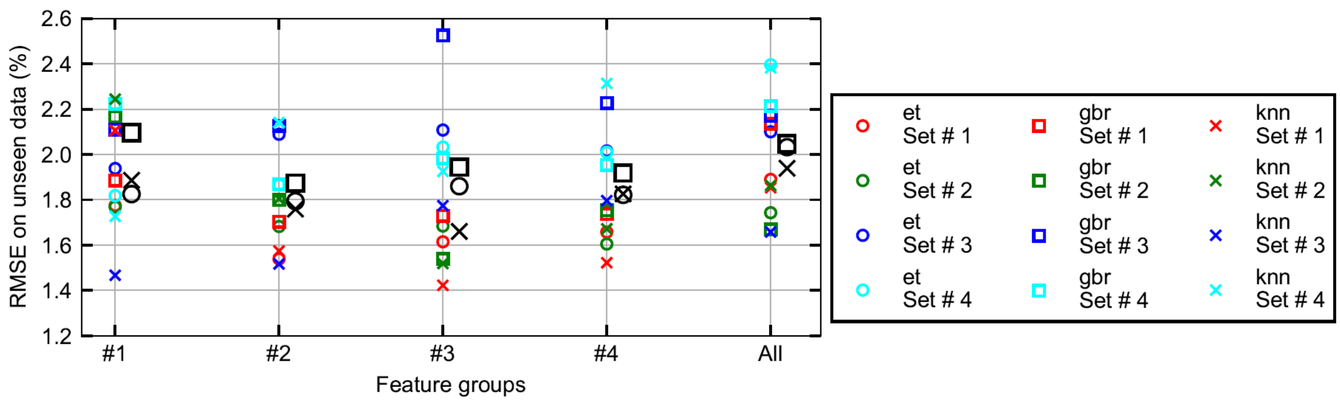

Figure 13- Summary of RMSE results on area reduction for four different feature selections.

In this case, limiting the model input to specific predictor groups while retaining all microstructural features types could improve the model performance slightly. Compared to the reference feature set including all available predictors, the ones using the d_{32} indicators or the d_{32} and 95th percentile along with shape characteristics and area occupation showed reduced RMSE, respectively. The set-to-set scatter also remains large. On the other hand, keeping only average size and area occupation (# 1) or relying on the absolute maximum sizes (# 4) did not improve the score. It should also be noted that the different unseen datasets do not react all in the same way to feature selection, which suggests that a deeper investigation into the critical predictors for correlations would be required.

CONCLUSION

In this work, a digital workflow was developed and tested to quantitatively characterize the microstructure of a high-pressure die-cast Al-Si-Mg-Mn alloy and then use this data in a machine learning framework to estimate the local yield strength and ductility. The applications envisioned were the characterization of difficult-to-measure regions such as rib crossing or small features that are often part of die-cast components or the gradients arising from the skin effect, as well as future integration with process simulations predicting microstructural characteristics for new casting designs.

The minimum predictive error in terms of RMSE was on the order of 5 MPa for yield strength. Area reduction at break was however less accurately predicted from the microstructural features with a RMSE on the order of 1.75%. In both cases, this represents approximately 11% of the measured property range, but the R^2 values were generally lower for ductility. This is not unexpected, given that ductility is likely to be more significantly affected by fewer, local features in the material. The lower predictive performance for ductility could for instance be due to the selection of a single cross-section plane which could miss significant features, as some specimens exhibited defects on the fracture plane. Another hypothesis is that features that are important to the mechanical properties are missing from the predictors set: some of these features may be at too small a scale to capture efficiently with optical imaging in a large-volume workflow.

The key microstructural features identified by the models were still generally consistent with the literature, showing that a more homogeneous and finer microstructure generally resulted in higher strength and ductility. Results should however be interpreted with caution, as the models seek correlations that are not necessarily causations. For instance, many predictors are related to the cooling rate and solidification time [7,17,48,52], which leads to correlated predictors. Machine learning algorithms may swap such correlated predictors.

In this work, casting parameters were varied and process data was collected, but neither were used as predictors in the correlation effort. Process to properties relationships are evaluated in a distinct modelling framework not shown herein. Apelian and Kopper highlighted that each machine and cavity combination can represent a unique process [38], which was a challenge for generalization of process-properties relations. On the other hand, the microstructure is expected to have a unique relationship to properties for a given material. A single, simple casting was used but work is underway to expand this framework to a more geometrically complex prototype with the same alloy to evaluate the transferability of the model to new cast components.

ACKNOWLEDGMENTS

This work was carried out as part of projects supported by the NRC's METALTec industrial research group as well as the Centre Québécois de Recherche et Développement sur l'Aluminium (CQRDA) and Canadian Office for Energy Research and Development (OERD). The authors would like to thank Dr Dominique Bouchard for in-depth discussions on aluminium metallurgy. The authors also wish to acknowledge the contributions of the NRC team who participated in the various aspects of this study: Dany Drolet, Mario Patry, Michel Perron, Alexandre Morin, Myriam Poliquin, Richard Desnoyers, Geneviève Simard, Martin Pruneau, and Keven Lepage-Potvin, as well as the METALTec industrial research group members who supported this investigation and publication.

REFERENCES

1. Otarawanna, S., et al., "Microstructure formation in AlSi4MgMn and AlMg5Si2Mn high-pressure die castings". *Metall Mater Trans A*. **40**: pp. 1645-1659 (2009).
2. Wang, Q.G., et al., "Size effects in aluminium alloy castings". *Acta Mater*. **58**: pp. 3006-3013 (2010).
3. Guan, R.-G. and D. Tie, "A review on grain refinement of aluminum alloys: progresses, challenges and prospects". *Acta Metall Sin*. **30**(5): pp. 409-432 (2017).
4. Osório, W.R., et al., "Effect of dendritic arm spacing on mechanical properties and corrosion resistance of Al-9wtpct Si and Zn-27wtpct Al alloys". *Metall Mater Trans A*. **37**: pp. 2525-2538 (2006).
5. Irfan, M.A., et al., "Porosity reduction and mechanical properties improvement in die cast engine blocks". *Mater Sci Eng A*. **535**: pp. 108-114 (2012).
6. Li, X., S.M. Xiong, and Z. Guo, "On the tensile failure induced by defect band in HPDC of AM60B magnesium alloy". *Mater Sci Eng A*. **674**: pp. 687-695 (2016).
7. Chadha, G., J.E. Allison, and J.W. Jones, "The role of microstructure on ductility of die-cast AM50 and AM60 magnesium alloys". *Metall Mater Trans A*. **38**: pp. 286-297 (2007).
8. Sun, X., K.S. Choi, and L.D. S, "Predicting the influence of pore characteristics on ductility of thin-walled high pressure die casting magnesium". *Mater Sci Eng A*. **572**: pp. 45-55 (2013).
9. Lee, S.G., et al., "Quantitative fractographic analysis of variability in the tensile ductility of high-pressure die-cast AE44 Mg-alloy". *Mater Sci Eng A*. **427**: pp. 255-262 (2006).
10. Rettberg, L.H., et al., "Low-cycle fatigue behavior of die-cast Mg alloys AZ91 and AM60". *Metall Mater Trans A*. **43**: pp. 2260-2274 (2012).
11. Liu, R., et al., "Influence of pore characteristics and eutectic particles on the tensile properties of Al-Si-Mn-Mg high pressure die casting alloy". *Mater Sci Eng A*. **783** (2020).
12. Lados, D.A., et al., "Microstructural mechanisms controlling fatigue crack growth in Al-Si-Mg cast alloys". *Mater Sci Eng A*. **468-470**: pp. 237-245 (2007).
13. Cinkilic, E., et al., "A formation map of iron-containing intermetallic phases in recycled cast aluminum alloys". *Metall Mater Trans A*. **50**: pp. 5945-5956 (2019).
14. Dinnis, C.M., J.A. Taylor, and A.K. Dahle, "As-cast morphology of iron-intermetallics in Al-Si foundry alloys". *Scripta Mater*. **53**: pp. 955-958 (2005).
15. Okayasu, M., et al., "Influence of microstructural characteristics on mechanical properties of ADC12 aluminum alloy". *Mater Sci Eng A*. **592**: pp. 189-200 (2014).
16. Lu, L., et al., "Eutectic solidification and its role in casting porosity formation". *J Mater*: pp. 52-58 (2004).
17. Ji, S., et al., "Effect of iron on the microstructure and mechanical property of Al-Mg-Si-Mn and Al-Mg-Si diecast alloys". *Mater Sci Eng A*. **564**: pp. 130-139 (2013).
18. Matthew, J., et al., "Effect of Fe intermetallics on microstructure and properties of Al-7Si alloys". *J Mater*. **71**(12): pp. 4362-4369 (2019).
19. Li, X., S.M. Xiong, and Z. Guo, "Improved mechanical properties in vacuum-assist high-pressure die casting of AZ91D alloy". *J Mater Process Technol*. **231**: pp. 1-7 (2016).
20. Tsumagari, N. and C. Mobley, "Microstructural characteristics of aluminum-silicon alloy die castings". 1993, The Ohio State University. p. 69.
21. Jiao, X.Y., et al., "Characterization of externally solidified crystals in a high-pressure die-cast AlSi10MnMg alloy and their effect on porosities and mechanical properties". *J Mater Process Technol*. **298** (2021).

22. Laukli, H.I., "High pressure die casting of aluminium and magnesium alloys - Grain structure and segregation characteristics". 2004, NTNU: Trondheim.
23. Zhang, J.Y. and Q. Han. "Microstructural features related to the choking of flow during HPDC". *NADCA die casting congress & tabletop*. 2019. Cleveland, OH.
24. Prakash, D.G.L. and D. Regener, "Micro-macro interactions and effect of section thickness of HPDC AZ91 Mg alloy". *J Alloys Compounds*. **464**: pp. 133-137 (2008).
25. Ridgeway, C.D., et al., "Prediction of location specific mechanical properties of aluminum casting using a new CA-FEA (cellular automaton-finite element analysis) approach". *Mater Des*. **194** (2020).
26. Kato, H., et al., "Nondestructive detection of cold flakes in aluminum alloy die-cast plate with ultrasonic measurement". *Mater Trans*. **45**(7): pp. 2403-2409 (2004).
27. Walkington, W.G. and M. Murray, "Die casting defects: causes and solutions (E-515)". 2015, North American Die Casting Association.
28. Watson, D., "Microstructure and mechanical properties of ductile die-cast Al-Mg-Si-Mn alloys". 2015, Brunel University London. p. 176.
29. Kopper, A.E., "Knowledge creation via data analytics in a high pressure die casting operation". 2020, Worcester Polytechnic Institute. p. 190.
30. Holm, E.A., et al., "Overview: Computer vision and machine learning for microstructural characterization and analysis". *Metall Mater Trans A*. **51**(12): pp. 5985-5999 (2020).
31. Gourlay, C.M., H.I. Laukli, and A.K. Dahle, "Segregation band formation in Al-Si die castings". *Metall Mater Trans A*. **35**: pp. 2881-2891 (2004).
32. Lordan, E., et al., "On the probabilistic nature of high-pressure die casting". *Mater Sci Eng A*. **817** (2021).
33. Gokhale, A.M. and G.R. Patel, "Analysis of variability in tensile ductility of a semi-solid metal cast A356 Al-alloy". *Mater Sci Eng A*. **392**: pp. 184-190 (2005).
34. Blondheim Jr, D. "Initial development of machine learning algorithms to predict casting defects in high-pressure die casting". *NADCA die casting congress & tabletop*. 2017. Atlanta, GA.
35. Blondheim Jr, D., "Unsupervised machine learning and statistical anomaly detection applied to thermal images". *Die Casting Engineer*(November): pp. 8-19 (2018).
36. Bhowmik, S. and D. Blondheim Jr, "Time-series analysis and anomaly detection of high-pressure die casting shot profiles". *Die Casting Engineer*(November): pp. 9-14 (2019).
37. Liu, F., et al. "AI-driven smart manufacturing of diecastings". *NADCA die casting congress & exposition*. 2018. Indianapolis, IN.
38. Apelian, D. and A.E. Kopper, "Predicting quality of cylinder block castings via supervised learning method". *Die Casting Engineer*(May): pp. 26-31 (2021).
39. Gu, C., et al., "Predicting grain structure in high pressure die casting of aluminum alloys: A coupled cellular automaton and process model". *Comput Mater Sci*. **161**: pp. 64-75 (2019).
40. Mao, H., "A numerical study of externally solidified products in the cold chamber die casting process". 2004, The Ohio State University. p. 178.
41. Forsmark, J.H., et al., "Using quality mapping to predict spatial variation in local properties and component performance in Mg alloy thin-walled high-pressure die castings: an ICME approach and case study". *Integrating Mater Manuf Innovation*. **4**(6) (2015).
42. Gariépy, A., et al. "Solidification model calibration for predicting microstructure fields in HPVDC Aural(TM)-2". *NADCA die casting congress & exposition*. 2021. Indianapolis, IN.
43. ISO, "ISO 6892-1 Metallic materials - tensile testing Part 1: method of test at room temperature". 2016.
44. Yang, K.V., et al., "The skin effect in high pressure die casting Al alloys", in *12th Int Conf Aluminium Alloys*. 2010: Yokohama, Japan. p. 687-692.
45. Chen, Z.W., "Skin solidification during high pressure die casting of Al-11Si-2Cu-1Fe alloy". *Mater Sci Eng A*. **348**: pp. 145-153 (2003).
46. Gourlay, C.M. and A.K. Dahle, "Dilatant shear bands in solidifying metals". *Nature*. **445**: pp. 70-73 (2007).
47. Easton, M., C. Davidson, and D. StJohn, "Grain morphology of as-cast wrought aluminium alloys". *Mater Trans*. **52**(5): pp. 842-847 (2011).
48. Prakash, D.G.L. and D. Regener, "Quantitative characterization of Mg17Al12 phase and grain size in HPDC AZ91 magnesium alloy". *J Alloys Compounds*. **491**(1-2): pp. 139-146 (2008).
49. Raymaekers, J. and P.J. Rousseeuw, "Transforming variables to central normality". *Machine Learning* (2021).
50. Lundberg, S.M. and S.-I. Lee. "A unified approach to interpreting model predictions". *31st conference on neural information processing systems*. 2017. Long Beach, CA.
51. Brancaleon, P., "Specifications and standards development for enhanced casting performance thru examination of mechanical properties versus casting section thickness". *Die Casting Engineer*(March): pp. 32-36 (2021).
52. Zhang, L.Y., et al., "Effect of cooling rate on solidified microstructure and mechanical properties of aluminium-A356 alloy". *J Mater Process Technol*. **207**: pp. 107-111 (2008).